PCCP

ROYAL SOCIETY OF CHEMISTRY

PAPER

View Article Online
View Journal

Cite this: DOI: 10.1039/d6cp00956e

On the effects of hyperpolarized water-based dissolution on the solute and solvent ^{1}H NMR spectra of small molecules

Dmitrii Aleshin,*[a] Korin Butbul,[a] Itai Hahamy,[a] Daniel Abergel[b] and Lucio Frydman *[a]

Received 15th March 2026,
Accepted 2nd May 2026

DOI: 10.1039/d6cp00956e

rsc.li/pccp

The exceptionally high spin polarizations that result from dissolution dynamic nuclear polarization (d-DNP), can lead to unusual liquid-state nuclear magnetic resonance (NMR) spectral features. This study analyzes such features, when performing d-DNP of hyperpolarized water to dissolve and sensitize the NMR spectra of co-dissolved molecules. Most evident among the collective spin effects that arise in such "HyperW" experiments is the very strong radiation damping (RD) affecting the water resonance. In addition, the presence of such strongly magnetized water signal alters both the amplitude and the phase of resonances emerging from the solutes co-dissolved in the hyperpolarized H_2O, for as long as these remain within the RD-broadened line width of water's resonance. These phase- and amplitude RD effects are superimposed on cross-relaxation and chemical exchange effects, which will also affect the phases and amplitudes of all peaks. Demonstrations and derivations of these effects, as well as a discussion of their consequences in HyperW experiments on solute-oriented measurements, are presented.

Introduction

Nuclear magnetic resonance (NMR) is widely used for probing molecular structure, dynamics, and interactions in physics,[1] chemistry,[2,3] biology,[4] and materials sciences.[5] Its unique strength lies in the ability to provide atomic-level information non-invasively and under near-physiological conditions. At the same time NMR is known to suffer from an intrinsically low sensitivity. This occurs in part due to the very small nuclear polarizations achieved by spin ensembles at room temperature, typically on the order of 10^{-4}–10^{-5} even at high magnetic fields. To overcome the ensuing weak signal intensities, "hyperpolarization" techniques have been developed capable of enhancing the NMR response of the targeted nuclei by orders-of-magnitude.[6] Methods such as parahydrogen-induced polarization (PHIP),[7] and spin-exchange optical pumping (SEOP)[8] have thus demonstrated significant gains in specific cases. Arguably, however, dynamic nuclear polarization (DNP)[9,10] has proven to be the most broadly applicable approach, with minimal restrictions on a substrate's chemical or physical properties. While originally constrained to observations on mostly cryogenically cooled solids,[11,12] the advent of the dissolution DNP (d-DNP) strategy[13] provided the versatility needed for hyperpolarizing high-field NMR and even MRI experiments, under room temperature and/or physiological conditions.[14,15] In d-DNP, nuclear spin polarization is first generated at cryogenic temperatures *via* a microwave irradiation driving an electron → nuclear polarization transfer. The hyperpolarized sample is then rapidly dissolved by a hot solvent and transferred into the NMR/MRI spectrometer, giving a transient state with significantly enhanced polarization. The effective enhancement that is achieved depends on the relaxation that spins will undergo upon being transferred from the hyperpolarizing to the NMR/MRI magnets, with relaxation losses getting more onerous for larger molecules like proteins or nucleic acids.[16] One variation that has been found useful to tackle these larger systems is the so-called "HyperW" approach,[17–37] which employs hyperpolarized water as a dissolution solvent. Being a small molecule, water's protons will preserve their DNP-imparted spin polarizations largely unhindered throughout the inter-magnet transfer; once biomolecules are dissolved in this highly polarized solvent, the water protons can transfer their hyperpolarization through chemical exchanges and/or nuclear Overhauser effects both to protons and to certain heteroatoms. This approach has yielded protein and nucleic acid 1D and 2D NMR spectra with sensitivity enhancements of up to three orders of magnitude compared to their conventional thermal NMR counterparts;[21,23–25,27,32,35,36]

[a] Department of Chemical and Biological Physics, Weizmann Institute of Science, Rehovot 7610001, Israel. E-mail: dmitrii.aleshin@weizmann.ac.il, lucio.frydman@weizmann.ac.il
[b] Chimie Physique et Chimie du Vivant – UMR 8228, Département de chimie, Ecole normale supérieure, PSL University, Sorbonne Université, CNRS, 75005 Paris, France

they have thus been applied in areas ranging from *in vivo* MRI[17,19,26] to protein structure determination,[25,29,31] from metabolomics[22] to binding.[20,28]

Despite this potential, HyperW experiments are not without challenges. A most evident feature associated to these experiments, are the large linewidths that can characterize the hyperpolarized water ^{1}H NMR resonance: when subject to small tip angle excitations, these can span several kHz regardless of shimming. This reflects the severe radiation damping (RD) arising in these experiments; *i.e.*, the collective interaction between water's large ^{1}H magnetization, and the NMR detection circuit. In these RD-dominated acquisitions, the water's free induction decay (FID) will generate a current in the detection coil, whose emitted radiofrequency (RF) field will act back on the spins.[38–47] This will drive hyperpolarized water's nuclear magnetization back towards the longitudinal z axis, as if it were an on-resonance pulse. Such RD effects have long been a feature of conventional NMR, particularly in 2D ^{1}H–^{15}N correlation experiments where high water concentrations are common;[48] however, under d-DNP conditions, the dramatically increased H_2O polarization will amplify conventional RD effects by orders-of-magnitude. These strong RD fields will evidently affect the water's spin dynamics; as here discussed and exemplified, such strong water RD fields will also influence the ^{1}H NMR signals of co-dissolved solutes, leading to frequency shifts and to offset-dependent phase distortions. In addition to these RD effects, the HyperW experiment will also significantly affect the overall intensities of the co-dissolved solute signals; part of this will result, as previously reported,[18,24,29,30] in large enhancements of labile solute protons that readily exchange with the hyperpolarized solvent. In addition, also non-labile protons can have their intensities changed by intermolecular cross-relaxation effects. These polarization transfer phenomena will interplay with the RD effects, leading to a non-trivial calculation of the actual signal enhancements. These and other features related to the solute's NMR in HyperW experiments are further described below – first with experimental examples, and thereafter with theoretical derivations accompanied by numerical simulations that explain these.

Experimental

Hyperpolarized water injections were performed by subjecting 100 μL aliquots of a glassy 8 : 2 H_2O/glycerol mixture containing 10 mM 4-aminoTEMPO, to microwave irradiation for 1 h at 1.6 K. The procedure was carried out in a 3.35 T Oxford Instruments HyperSense® polarizer, using 120 mW of microwave power positioned at 94.10 GHz. The hyperpolarized pellets were dissolved with 4 mL of superheated D_2O buffer, adjusted to pH 7 for the pyridine/propanol tests (aka. sample I) and to pH 3 for alanine-oriented experiments (sample II). The hyperpolarizer → NMR magnet transfer was aided by a stream of Helium gas pressurized to 10 bar, which transferred the hyperpolarized water into 5 mm NMR tubes within 8 s. Inside this 11.7 T NMR magnet, tubes with either 10 μL of 1 : 1 vol. pyridine/propanol mixture (sample I) or 150 μL of a 1 M alanine solution in D_2O (pH 3, sample II) were already waiting, inside a pre-shimmed triple-resonance Prodigy® Bruker probe. The probe was maintained at room temperature (25 °C) yet the transfer lines between the Hypersense and NMR magnets were kept at ≈45 °C, to lengthen the water ^{1}H T_1 times to ≥8 s. The final volume of the solution after the hyperpolarized water injection was controlled by an Arduino-based controller,[49] and set to reach a final total value of ≈470 μL. Repeated experiments indicated a net d-DNP enhancement of *ca.* 1200× for the water ^{1}Hs, *vs.* their thermal 11.7 T counterparts.

^{1}H NMR spectra were acquired from *ca.* 5 s prior to the hyperpolarized water arrival into the NMR tube, till *ca.* two minutes after its arrival. Acquisitions used a 500 MHz Bruker Neo console, and small-angle (3°) tip pulses calibrated and tuned on appropriate volumes of a H_2O/D_2O (10/90) sample; such sample was also used for a pre-dissolution shimming. Data were collected as pseudo-2D datasets with 200 free induction decays (FIDs), an acquisition time of 0.2 s per FID, a 0.4 s inter-FID delay, a spectral width of 30.12 kHz, and a spectrometer dead time of 10 μs. To avoid sweep-field correction artifacts, deuterium lock and sweep systems were deactivated during the dissolution process.

Results

Experimental observations

Fig. 1 shows 1D ^{1}H signal line shapes recorded upon dissolving 10 μL of 1 : 1 vol. pyridine/propanol in 460 μL hyperpolarized water. Panel (a) presents selected full-spectral-width small-tip-angle ^{1}H NMR spectra, illustrating the dramatic changes in linewidth that the water resonance experiences as a function of post-dissolution time. Most noticeable is this central peak's large symmetric line width, that gradually narrows in unison with a shift in the peak's maximum. Such broad line shapes are unrelated to B_0 inhomogeneities (which when present were usually due to the appearance of small bubbles leading to asymmetric peaks as expected from a z^2-like distortion along the main axis); instead, the exponential decay that both the width and the center of mass of the water line exhibit (Fig. 1b), are hallmarks of a RD-dominated behavior. Furthermore, the similar decay constants that are observed for these two decays and for the decay of water's overall hyperpolarization, supports a common origin for all these effects. Notice that immediately after dissolution, the water resonance exhibits a maximal shift of 400 Hz. Such large frequency excursion cannot be attributed to demagnetization fields (DFs), which for the cylinder in question should be around 35 Hz under typical HyperW conditions (see SI, Section S1). Furthermore, a DF would shift all resonances in the spectrum by a similar amount, whereas solute signals shift only by ∼40 Hz over the course of the post-dissolution. Neither can these shifts be explained by the 15 °C bulk temperature changes undergone with the water upon being ported from the polarizer to the NMR probe: when measured in ''dummy'' unpolarized water dissolutions, such shifts would not

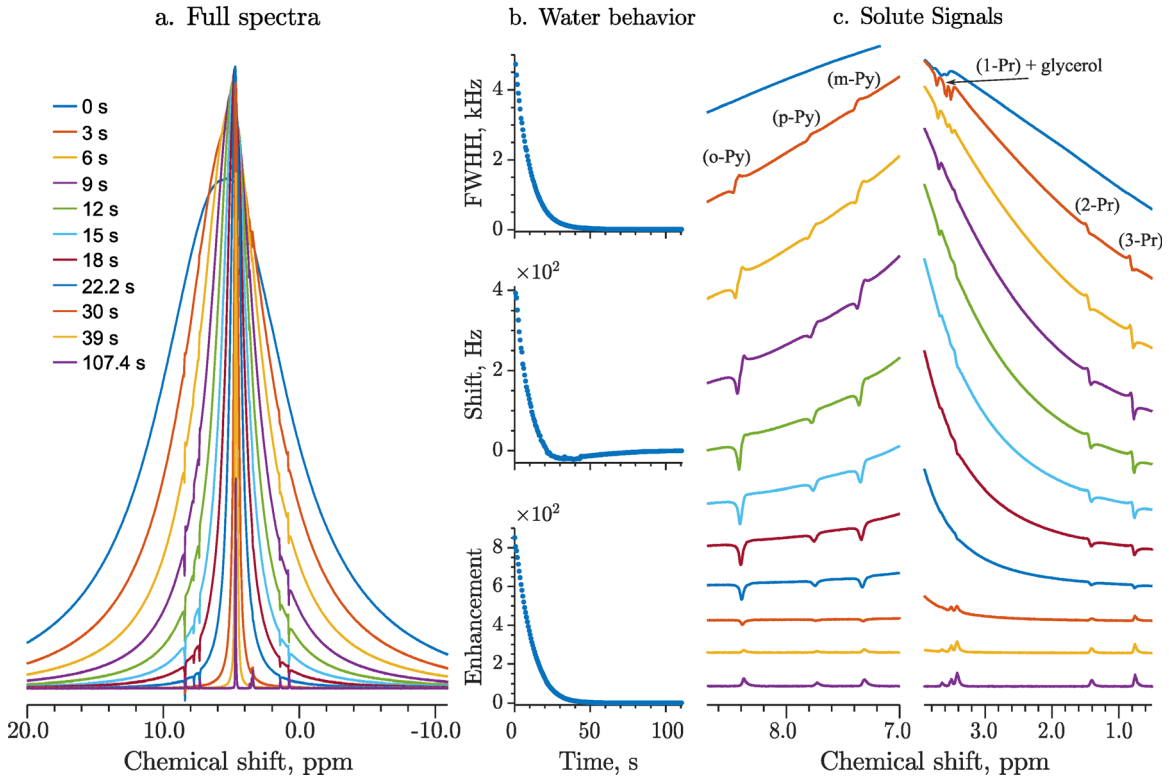

Fig. 1 ^{1}H NMR results observed upon injecting hyperpolarized water into a pyridine/propanol sample. (a) Small-tip-angle spectra, focusing on the water signal line shape changes following a dissolution reaching the NMR tube at time t = 0. (b) Summarizing the main water peak's changes – full width at the half height (FWHH), center of mass frequency shift, and enhancement over thermal at 11.7 T – arising for the water signal post-dissolution. While the dominant RD-induced shift masks temperature and demagnetization field effects at early times, gradual cooling of the sample manifests at $t > 20$ s as a slow reversal in the shift of the water resonance (center panel). (c) Zoomed-in plots highlighting changes in the solute signal line shapes following (labeled as Py and Pr for pyridine and propanol respectively) during the HyperW dissolution. Colors correspond to the post-dissolution times shown in panel (a); spectra have been horizontally zoomed and vertically displaced for easier appreciation of the solute resonances, while cropping out the center water peak region. However, the same vertical scale was used for all traces in the series.

exceed a few tens of Hz. On the other hand, water's 400 Hz exponentially decaying shift is fully consistent with a frequency-pushing arising from RD, as further discussed in the next section.

While also showing a marked post-dissolution time dependence, the solute resonances highlighted in Fig. 1c from propanol and pyridine, resonating respectively at 0.75, 1.4, 3.4 and at 7.31, 7.73 and 8.37 ppm values, behave quite differently from the water peak (≈4.8 ppm). In the initial post-dissolution traces these solutes are virtually invisible. Within the first 5 s or so their ^{1}H NMR signature grows, but their peaks appear out-of-phase vs the water; in fact, they show opposite phases depending on whether they resonate at higher or lower offsets *vis-à-vis* the water. As RD decreases sufficiently for the water peak to stop overlapping with the solutes (≈10–20 s post-dissolution) peaks still show-up magnified, but now they have evolved into a common phase; a phase that is 180° shifted from that of the water. Finally, once the water ^{1}Hs have reached thermal equilibrium (post-dissolution times >40 s) the solutes show conventional, positively-phased, J-split absorptive line shapes (Fig. 1c, bottom).

We ascribe the unusual solute phase behavior to the effect of water's RD field acting on these protons; as further described below this will – if large enough – impart phase peak shifts depending linearly on a site's (signed) offset relative to the water resonance. Consequently, solute resonances with opposite offsets relative to the water signal will accrue phases of opposite sign for as long as RD can act on their evolution – *i.e.*, for as long as the water line overlaps with the solute resonances. Added on top of these RD effects is an intermolecular cross-relaxation that, for the case of small molecules like the ones being here considered, will lead to a negative nuclear Overhauser enhancement (NOE) between the hyperpolarized water protons and the non-labile propanol/pyridine protons – regardless of RD effects.[2,4] This NOE naturally ceases once the water spins have reached thermal equilibrium, and therefore solutes and water return to a fully positive NMR trace.

Fig. 2 presents another representative dissolution, this time for an alanine sample dissolved on hyperpolarized water. For all practical purposes, the water in these small-tip-angle experiments behaves identically as in the HyperW counterpart of Fig. 1. However, the labile amino protons in this case are enhanced much more than the non-labile methyl protons due to exchange-driven interchange with the hyperpolarized water protons, leading to a positive magnetization for the $-NH_3^+$ and to a negative NOE for the CH_3. Still, since the phase-distortions

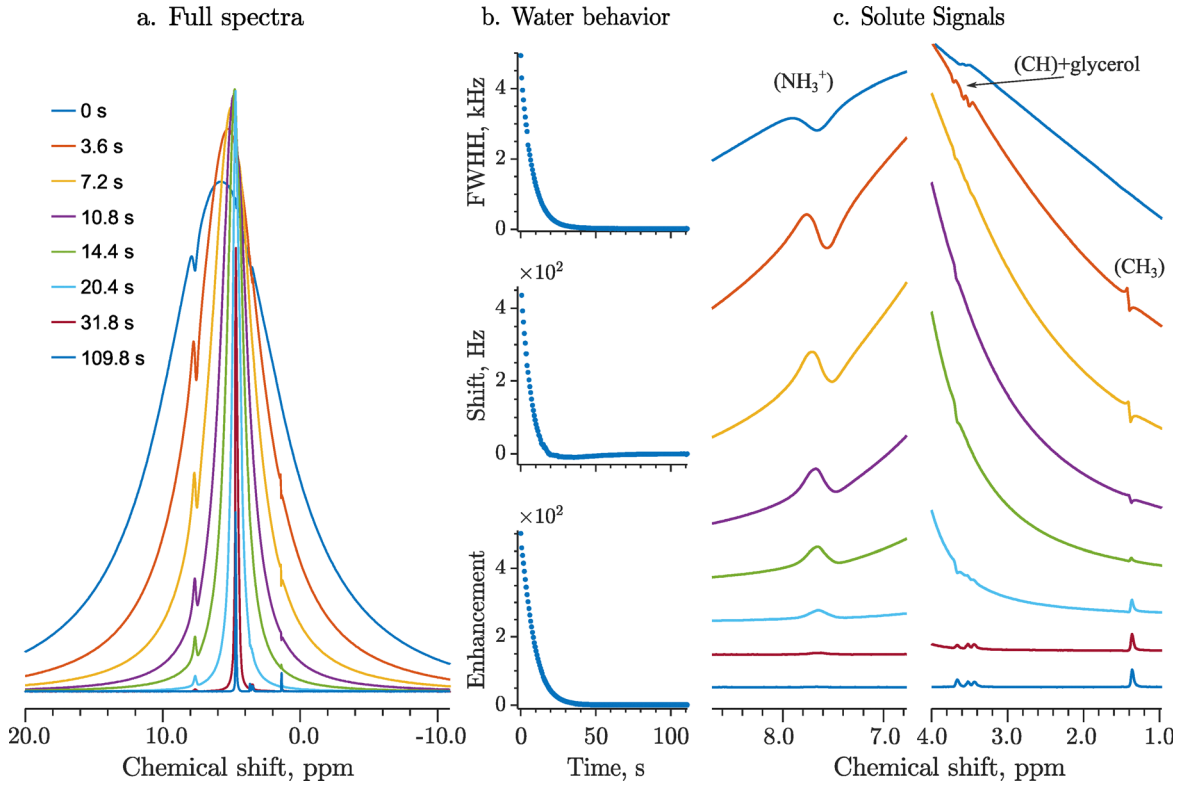

Fig. 2 Idem as in Fig. 1, but for ^{1}H HyperW NMR experiments performed using alanine as the solute (sample II).

imposed by water's RD effect are as in sample I, the ensuing phase distortion ends up having the same phase sign for both solute ^{1}H signals: the enhancements of the CH_3 and $-NH_3$ magnetizations have now different signs, but so do their relative offsets *vis-à-vis* the water. Complicating somewhat the clear observation of this effect, is the fact that the amine protons are substantially broadened by their exchange with the water, as well as by relaxation of the second kind with the ^{14}N. This extra broadening makes the NH_3 peak nearly invisible once protons have returned to thermal equilibrium.

Understanding and reproducing water's overall behavior

In the HyperW experiments above, a ≈0.1mL aliquot of hyperpolarized water is flushed by ≈4mL of overheated D_2O to an Arduino®-controlled pressurized system, which in turn transfers a fraction of the ensuing mixture into the NMR tube. While in such 11.7 T NMR experiments the water ^{1}H signal was enhanced *ca.* 1000-fold (higher enhancements could be achieved when bypassing the pressurized dissolution system yet at the expense of some foaming), the flushing with D_2O dilutes the initial proton concentration. According to repeated color dye experiments the dilution factor is large, *ca.* 20×; still, the effective proton magnetization in these experiments is *ca.* 40–50 times larger than that of tube full of pure H_2O placed in an 11.7 T magnet. Such strong nuclear magnetization will, particularly when considering the high B_0 homogeneity and the cryogenic-coil setup used in our experiments, create conditions where RD and/or DF effects, cannot be neglected.[50] For a cylindrical 5 mm tube with water at thermal equilibrium, the DF created by the water polarization can be estimated from Boltzman's equation for nuclear paramagnetism: in an 11.7 T field at 300K this should amount to ≈0.7 Hz (see SI Section S1). While under HyperW conditions this value will rise 40- or 50-fold, it still cannot explain the ≈400 Hz center-of-mass water shifts observed in Fig. 1b and 2b. Further, if DF were the source of the observed water shifts, the same displacement should affect all remaining signals in the sample; as none of these is observed, the dominance of DF can be discounted. Another factor to consider is temperature: the hyperpolarized water solution is flushed out from the polarizer at *ca.* 35 °C, and is heated on the way to the NMR tube to about 40 °C to lengthen the ^{1}H's T_1. As the NMR sample is being kept at *ca.* 25 °C in the probe, the hyperpolarized water will cool down over time; given water's −0.01 ppm $°C^{-1}$ temperature dependence, this might also bring about a water-specific chemical shift displacement. Such expected cooling, however, should shift H_2O's (and in a nearly identical fashion, HDO's) peak to higher ppm values,[51] which is opposite to the main displacement undergone by the water in Fig. 1 and 2. Such residual cooling effects cannot thus explain water's main post-dissolution shifts – even if they are observable (Fig. 1b and 2b; >20 s post-dissolution times in the "Shifts" plots) as small displacements towards slightly higher ppm values, after water's hyperpolarization has largely decayed to thermal values.

In view of all this, we ascribe the main broadenings and shifts observed on the water peaks in these experiments, to RD effects. As mentioned, RD originates from feedback between

the currents induced by the nuclear magnetization and the RF fields that these generate within the NMR probe detection circuit.[38–47] In the lab-frame, these FID-induced magnetic fields can be expressed as:[38]

$$\vec{B}_{\mathrm{RD}}(t) = -\frac{\mu_0 \eta Q}{\omega_{\mathrm{LC}}\sqrt{1+\Delta_{\mathrm{LC}}{}^2}} e^{i\psi} \frac{\mathrm{d}M_x(t)}{\mathrm{d}t} \vec{e}_x \qquad (1)$$

Here μ_0 is permeability of free space; η is the coil filling factor; Q is the quality factor of the receiving LC-circuit; $\Delta_{\mathrm{LC}} = Q\frac{\omega^2 - \omega_{\mathrm{LC}}{}^2}{\omega\omega_{\mathrm{LC}}}$ is a parameter defining the miss-tuning of the receiving circuit, with ω and ω_{LC} being the spins Larmor and the probe's LC-circuit resonance frequencies, respectively; ψ = arctan (Δ_{LC}) is a phase that the RD-induced field develops because of this miss-tuning; and the linearly polarized receiving coil is supposed to be aligned along the $\vec{e}_x$-axis (perpendicular to B_0). The RD field in eqn (1)[38] will act back on the spins, with a torque given by an angular rate constant $R_{\mathrm{RD}} = \lambda_{\mathrm{RD}} M_z$, where M_z is the magnitude of the z-magnetization at the time of excitation, and $\lambda_{\mathrm{RD}} = \frac{\mu_0 \eta Q \gamma \omega_0}{\omega_{\mathrm{LC}}\sqrt{1+\Delta_{\mathrm{LC}}{}^2}} e^{i\psi}$. When this feedback field is included, the resulting rotating-frame Bloch equations become:[52]

$$\begin{aligned}
\frac{\mathrm{d}M_x}{\mathrm{d}t} &= -\Delta\omega M_y + \frac{M_z|\lambda_{\mathrm{RD}}|}{2}\left(-M_x\cos(\psi) + M_y\sin(\psi)\right)\\
\frac{\mathrm{d}M_y}{\mathrm{d}t} &= \Delta\omega M_x - \frac{M_z|\lambda_{\mathrm{RD}}|}{2}\left(M_y\cos(\psi) + M_x\sin(\psi)\right) \qquad (2)\\
\frac{\mathrm{d}M_z}{\mathrm{d}t} &= \frac{\left(M_x{}^2 + M_y{}^2\right)|\lambda_{\mathrm{RD}}|}{2}\cos(\psi)
\end{aligned}$$

For a perfectly tuned probe ψ = 0;† $\vec{B}_{\mathrm{RD}}$ will then remain orthogonal to the transverse magnetization $M_\perp$, acting like a soft RF pulse which nutates the magnetization back to the z-axis (Fig. 3a). As this reduces the transverse magnetization,[39] RD is usually associated to a rapid FID transverse decay whose angular rate given by $\frac{M_0|\lambda_{\mathrm{RD}}|}{2}\cos(\psi)$ – even if, unlike T_2, this "rate" will not lead to a constant exponential function as its effects depend on the excitation and on the instantaneous tilt angle.[53] This notwithstanding R_{RD} gives an idea of the strength of RD effects; for typical probe filling factors η (0.07[44])and cryoprobe quality Q factors (600–700[44,45]), the expected value under the HyperW conditions and small-pulse excitation described above should be

$$\frac{R_{\mathrm{RD}}}{\pi} \approx \mathrm{FWHH} \approx \frac{\mu_0}{2\pi}\gamma\eta Q M_{\mathrm{HyperW}} \approx 5\,\mathrm{kHz} \qquad (3)$$

RD can thus broaden the water signal into the 10 ppm range observed in Fig. 1 and 2, clearly dominating over DF effects.

The phase shift ψ in the equations above will be different from zero if the probe is slightly detuned; *i.e.*, if there is a difference between the water Larmor and the maximal induced current impedance frequencies. This will move $\vec{B}_{\mathrm{RD}}$ away from orthogonality *vis-à-vis* $\vec{M}_\perp = M_x + iM_y$, leading to so-called "cavity pushing" effects[45,54] which manifest as M-dependent frequency shifts of the signal. Indeed, in a Bloch-sphere rotating frame picture, RD-induced rotations will then occur around $\vec{B}_{\mathrm{RD}}$ fields that are no longer orthogonal to $\vec{M}_\perp$, producing an additional, time-dependent effective rotation around the z-axis (Fig. 3). Notice that owing to the metastable nature of d-DNP experiments, these "pushing" effects will not be constant throughout the HyperW post-dissolution series, but rather diminish with the decaying magnetization.

The aforementioned RD-based arguments explain, *via* the hyperpolarization-dependent post-dissolution R_{RD} values, most of the exponentially decaying water line widths and shifts summarized in Fig. 1b and 2b. However, obtaining a more perfect fit between these expectations and the results presented in Fig. 1 and 2, required invoking additional factors. These included the aforementioned, magnetization-dependent demagnetizing field and time-dependent water-cooling effects, which were accounted as described in more detail in the SI Section S1. Also in need of accounting was the fact that, given the strong RD effects arising in HyperW experiments, the loss of the initial part of the FID as imposed by the spectrometer's dead time, strongly influenced the apparent signal enhancement – and therefore the quantitation of the water signal as a function of time. Indeed, given a characteristic decay time $(R_{\mathrm{RD}})^{-1} \approx 60$ μs, a spectrometer dead time of ≈10 μs meant that ≈20% of the signal was effectively lost by the time of the data acquisition. These losses accounted for the non-exponential behavior that had been previously noted for integral-derived estimations of the post-dissolution HyperW enhancements;[18,42,55] the data in Fig. 1 and 2 also show similar non-exponential apparent decays for the water hyperpolarization. Fig. 4 shows the increased initial water enhancements, arising when extrapolating back the best-fits of the hyperpolarization decay emerging from longer (≥10 s) post-dissolution times. These increased enhancements reflect the fact that the initial post-dissolution scans are subject to larger RD-induced polarization decay rates R_{RD}, and hence so are their signal losses during the spectrometer's dead time. As the hyperpolarization decays and RD effects become smaller so do dead-time related losses, until eventually becoming negligible. To ensure quantitative accuracy, the influence of the spectrometer dead time therefore had to be explicitly accounted for.

With all these provisions, numerical simulations based on eqn (2) could reproduce the experimental water line shape well (Fig. 5). The fitting parameters that these Bloch model required for recapitulating the examples in Fig. 1 and 2 included DNP enhancements of 1170 and 680, and ψ values of 10.2° and 11.5°, respectively. Achieving the close agreement between expectations and experiments shown in Fig. 5, also called for an unexpected, ≈2% variation of $|\lambda_{\mathrm{RD}}|$ over the initial (≈ 6 s) post-dissolution periods. This variation was modeled as‡

$$|\lambda_{\mathrm{RD}}(t)| = \lambda_0 + \Delta\lambda_{\mathrm{RD}}\left(1 - e^{-\frac{t}{\tau}}\right) \qquad (4)$$

† In ref. 52 ψ is the angle between the feedback field and the transverse magnetization, whereas here it is being used as a phase related to the detuning. Both are simply related by a 90° difference.

‡ Also the phase ψ should show changes upon dissolution; however, to first order these can be included in a redefinition of the λ_0.

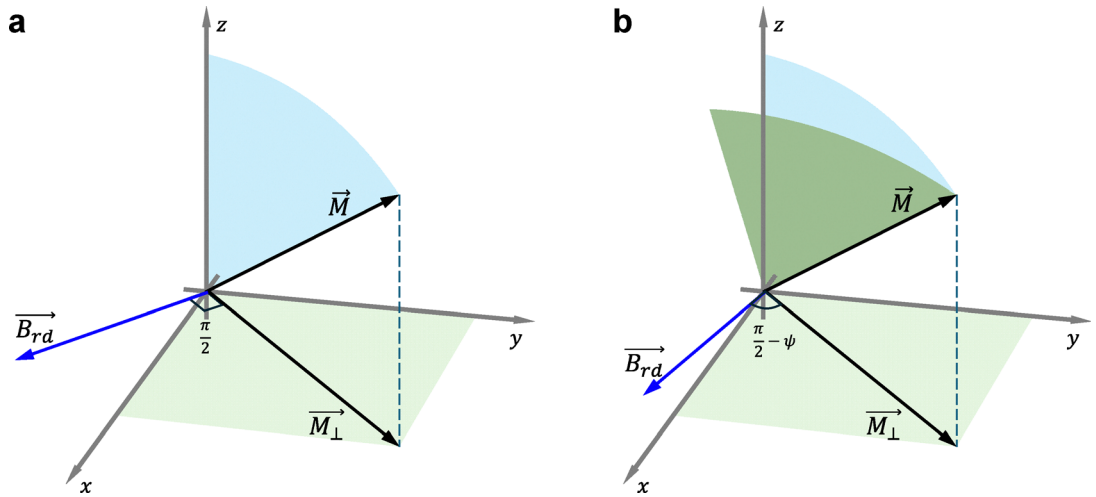

Fig. 3 Schematic representation of how a radiation damping field $\vec{B}_{RD}$ influences the torque exerted by RD on the sample magnetization $\vec{M}$. (a) Case for $\psi = 0°$; the blue surface shows magnetization trajectory under the influence of radiation damping field, contained in the (z, $\vec{M}_\perp$) plane. (b) Case of $\psi \neq 0°$, showing a magnetization trajectory that departs slightly from the z-axis.

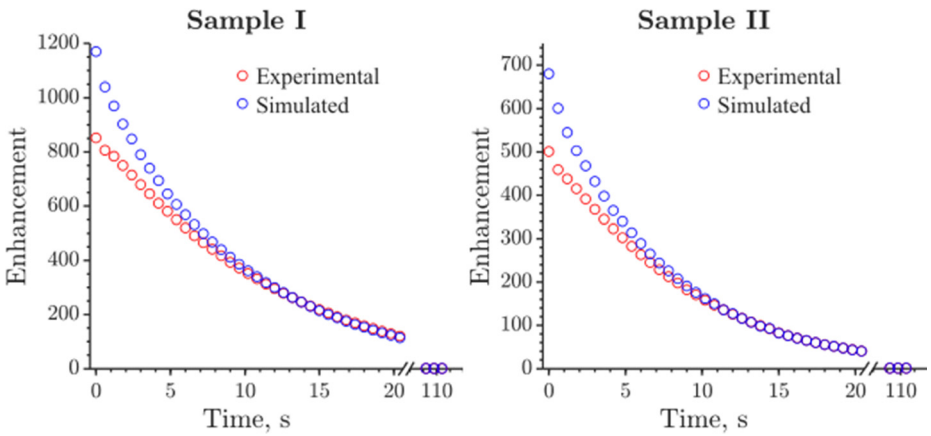

Fig. 4 Experimental and back-extrapolated enhancements observed for water in Fig. 1 and 2, as a function of post-dissolution time. Blue circles account for a 10 μs dead-time correction of the water enhancements, as derived from the water line-shape simulations in Fig. 5.

and it was tracked down to the changes that the probe's tuning and effective η/Q factors undergo, upon initially filling the tube with hyperpolarized water. Indeed, as exemplified in SI Fig. S3, S4 and S5 taken from snapshots of the system's "wobble" while performing a HyperW experiment (full videos downloadable as part of the SI), sizable perturbations affected the LC-receiving circuit upon doing the dissolutions. While the ^{1}H wobble traces were dominated by a strong "spike" in their center arising from significant RF absorption by water's hyperpolarized protons, variations were clearly visible when looking at the probe's ^{1}H channel tuning. (These are shown in the SI *via* tuning changes affecting the ^{19}F coil reflection, which had a close frequency and displayed effects that were qualitatively to the ^{1}H channel). Such measurements showed a clear perturbation of the probe during first second post-dissolution, suggesting $\tau \sim 4$ s for eqn (4). These changes in the probe tuning affected the degree and shape of the RD; with this final ingredient, the simulations displayed in Fig. 5 were obtained.

Understanding and reproducing the solutes NMR behavior

It follows that the B_{RD} field will act like an FID-induced RF pulse lasting for a time $(R_{RD})^{-1}$. According to time-frequency reciprocity principles, this means that B_{RD} will affect all signals within a $\pm R_{RD}/2$ frequency interval; *i.e.*, all peaks overlapping with the RD-active water resonance.[43] This phenomenon, together with intermolecular chemical exchange and cross-relaxation effects, becomes far more pronounced under HyperW conditions than in conventional NMR. To understand how these effects manifest in the solute spectral features shown in Fig. 1 and 2, we focus first on the out-of-phase line shapes that solutes display when water's RD-broadened peak overlaps with them. Notice that these phase-twists disappear as water narrows and returns to thermal equilibrium. Since the data in Fig. 1 and 2 were collected utilizing small tip angles, we can assume that at any given time the water longitudinal magnetization M_z^w equals water's overall magnetization M^w, which starts hyperpolarized and will decay over a time T_1 to thermal equilibrium. Likewise, we assume that the solute's

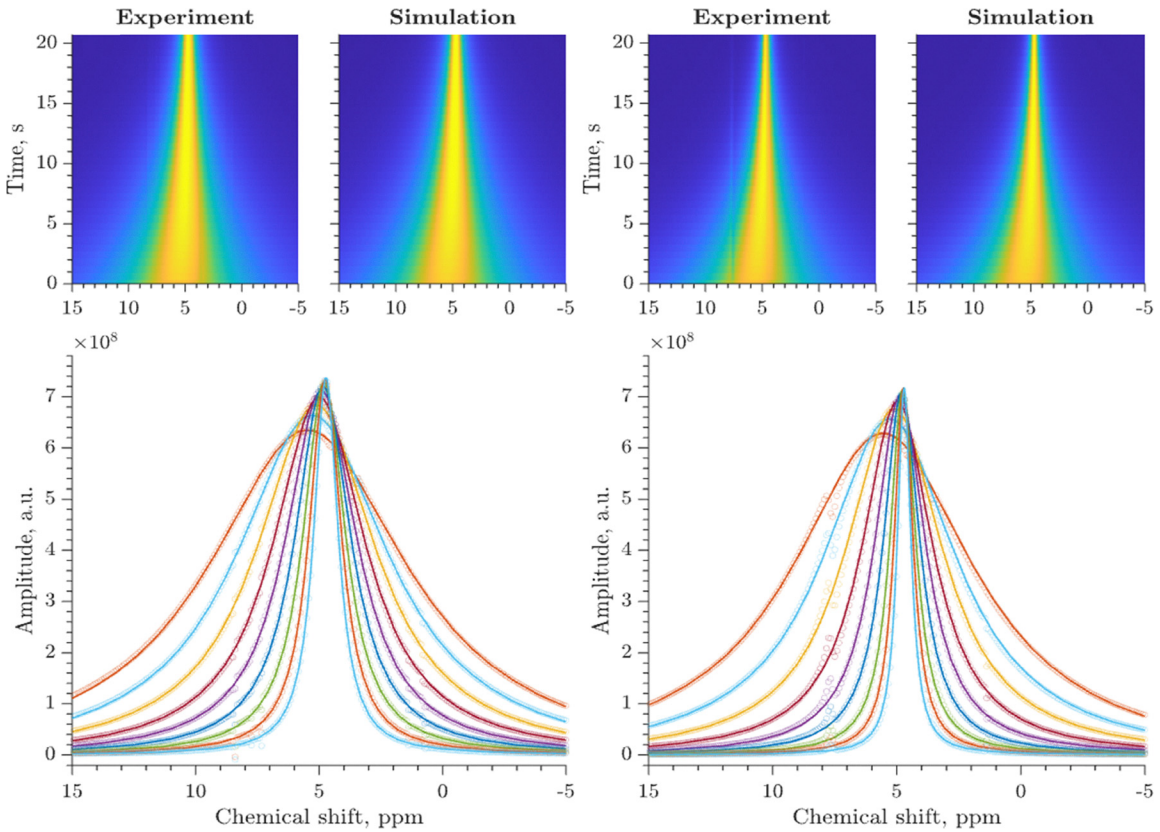

Fig. 5 Experimental and simulated water data corresponding to the dissolutions shown in Fig. 1 (left) and Fig. 2 (right). Experimental and simulated plots are shown as heatmap (top) and spectra (bottom). In the latter, simulated spectra (lines) are superimposed on experimental data (circles, shown sparsely every 90 points), and are displayed for post-dissolution times starting at 0.6 s, and with 2.4 s interval.

magnetization $M_z^s \approx M^s$. Assuming for the water signal an on-resonance irradiation and neglecting for the moment anything but the water RD, the coupled Bloch equations[43] for a water–solute system can be written as:

$$\frac{dM_+^w}{dt} = -\delta \cdot M_+^w - \delta \cdot M_+^s \quad (5a)$$

$$\frac{dM_+^s}{dt} = i\Delta\omega M_+^s - \frac{\delta}{M_z^w} \cdot M_+^w M_z^s \quad (5b)$$

where $\delta = \frac{\lambda_{RD}}{2} M_z^w$, and superscripts w, s denote the water and solute spins, respectively.

Given that the solute magnetization is much smaller than that of water, $M_z^s/M_z^w \ll 1$, eqn (5) will contain very rapidly and more slowly decaying terms. For instance $-\delta \cdot M_+^w$ and $-\frac{\delta}{M_z^w} \cdot M_+^w M_z^s$ will induce an initial fast decay, but their influence on the precessing M_+^s solute FID which originate the peaks in Fig. 1 and 2 can, to zero order be neglected. In fact, to 0th order, only the dominant RD term acting on the water magnetization and the usual precession of M_+^s matter. To such order, eqn (5) can be solved to retrieve these two transverse magnetizations as

$$M_+^w(t) = M_+^w(0)e^{-\delta \cdot t} \quad (6a)$$

$$M_+^s(t) = M_+^s(0)e^{i\Delta\omega t} \quad (6b)$$

To first order, however, the solute signal also experiences the effect of the RD-active magnetization *via* the $-\frac{\delta}{M_z^w} \cdot M_+^w M_z^s$ term: this represents a perturbation caused by water's RD on the solute. Conversely, assuming all experiments were done with small-tip-angle but broadband pulses, the ensuing $\frac{M_z^w(t=0)}{M_z^s(t=0)} = \frac{M_+^w(t=0)}{M_+^s(t=0)}$ relation means that $M_+^w(0)M_z^s \approx M_+^s(0)M_z^w$; *i.e.*, that also the $-\frac{\delta}{M_z^w} \cdot M_+^w M_z^s$ term may provide a contribution to the detected M_+^s to the same order. To derive such potential higher-order effects we look for general solutions of a first-order-revised version of eqn (5b):

$$\frac{dM_+^s}{dt} = i\Delta\omega M_+^s - \delta \cdot M_+^s(0)e^{-\delta \cdot t} \quad (7)$$

This can be solved using a Green-function expansion

$$M_+^s(t) = M_+^s(0)e^{i\Delta\omega t} - \delta \cdot M_+^s(0)e^{i\Delta\omega t}\left(\int_0^t e^{-(i\Delta\omega+\delta)\tau} d\tau\right) \quad (8a)$$

$$= \frac{M_+^s(0)}{\delta + i\Delta\omega}\left(\delta e^{-\delta t} + i\Delta\omega e^{i\Delta\omega t}\right) \quad (8b)$$

$$\approx \frac{M_+^s(0)}{\delta + i\Delta\omega} i\Delta\omega e^{i\Delta\omega t} \quad (8c)$$

where the last line neglected the fast-decaying $\delta e^{-\delta t}$ term. Adopting a similar perturbative approach to approximate the water signal, it can be concluded that the latter also will have a slowly decaying component at offset $\Delta\omega$. Indeed, inserting eqn (8c) into eqn (5a)

$$\frac{dM_+^w}{dt} = -\delta \cdot M_+^w - \frac{\delta M_+^s(0)}{\delta + i\Delta\omega} i\Delta\omega e^{i\Delta\omega t} \quad (9)$$

leads to a correction which to first-order can be solved *via* the Green-function approach, as

$$M_+^w(t) = M_+^w(0)e^{-\delta t} - M_+^s(0)\frac{\delta \cdot i\Delta\omega}{(\delta + i\Delta\omega)^2}\left(e^{i\Delta\omega t} - e^{-\delta t}\right) \quad (10)$$

Disregarding again the fast-decaying $e^{-\delta t}$ terms in eqn (10) and collecting all the terms that in eqn (8) and (10) contribute to a solute precession frequency $\Delta\omega$, yields after some algebra to

$$M_+^s(t) = M_+^s(0)\left(\frac{i\Delta\omega}{\delta + i\Delta\omega}\right)^2 e^{i\Delta\omega t} \quad (11)$$

It follows from this expression that the phase of the observed solute signal is determined by a product of the evolving magnetization times a complex factor $\left(\frac{i\Delta\omega}{\delta + i\Delta\omega}\right)^2$, that will impart on the solute peaks phase distortions *vs.* a conventionally phased purely-absorptive peak, of $\pi - 2\arctan\left(\frac{\delta}{\Delta\omega}\right)$. Thus, if the peak

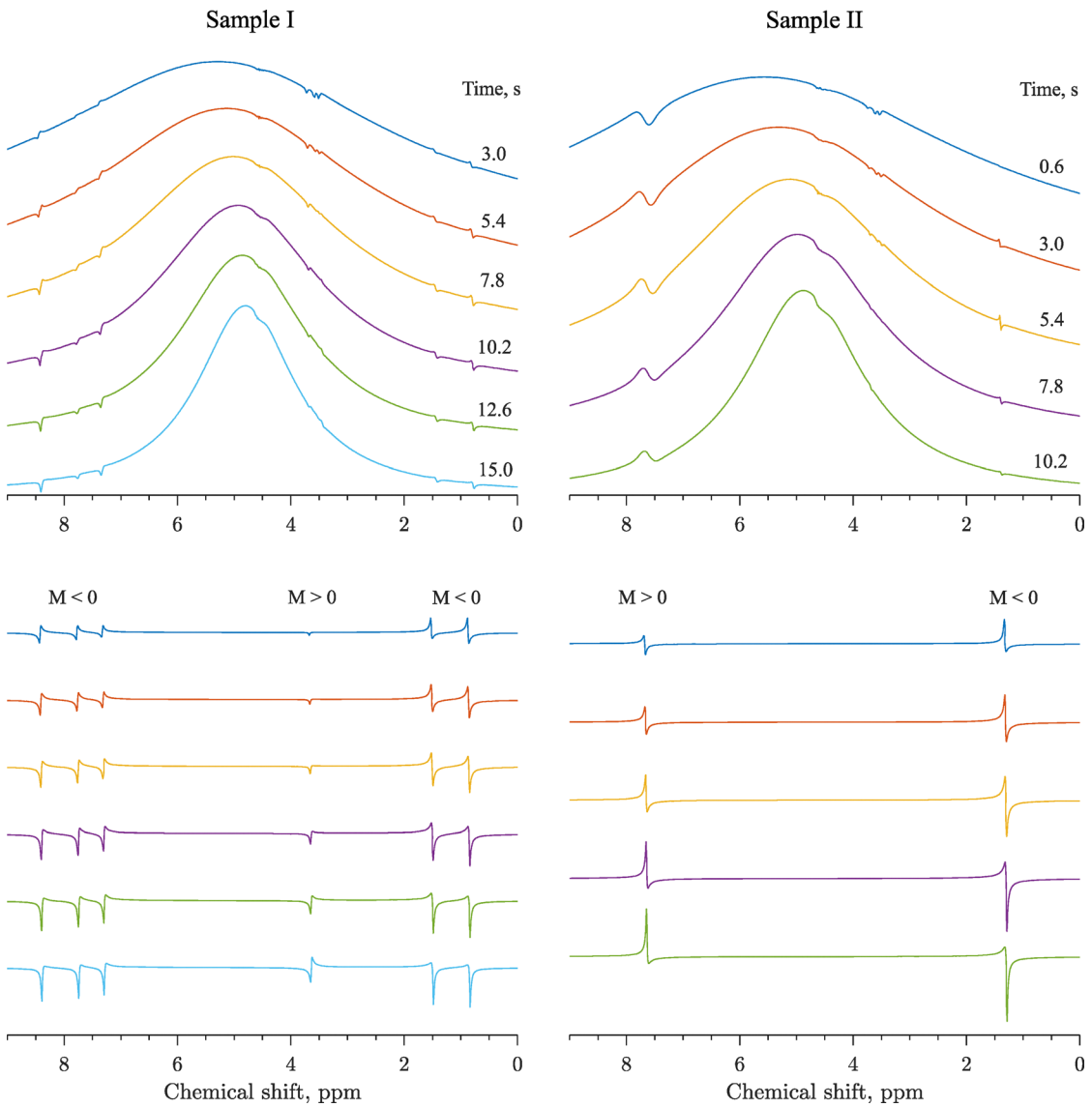

Fig. 6 Experimental (top) *vs.* analytically predicted (bottom) spectra focusing on the solute resonances appearing in Fig. 1 and 2. Analytical spectra were calculated based on eqn (11) after applying an apodization of 40 Hz. Solute magnetizations *M* were considered positive or negative as per exchange or NOE transfers from the hyperpolarized water (solutes) or from the direct hyperpolarization process (alanine's $-NH_3^+$ plus glycerol peak at ≈3.6 ppm). See text for further details.

offset exceeds the effects of the RD-broadened water $R_{RD} = \mathrm{Re}(\delta) = \frac{|\lambda_{RD}|}{2} M^{w} \cos(\psi)$, the phase distortion will be negligible; otherwise, the phase distortions of the solute peaks will be sizable, and have opposite signs on either side of the water peak. Fig. 6 presents simulations that, based on this analytical description and utilizing the values of λ_{RD} and M^{w} enhancement obtained in the previous Paragraph, are expected for the various solutes introduced in Fig. 1 and 2. Notice that these simulations kept fixed the offsets and the absolute magnitudes of the solute magnetizations, and attention was solely focused on predicting solute peak phases as a function of solvent hyperpolarization. Notice that these simulations also include one of glycerol's ^{1}H peaks which, despite arriving at the sample with a positive hyperpolarization, exhibits an inverted phase that generates "a hole" in water's RD-broadened peak, at the early post-dissolution stages. This transient phase inversion might be misassigned as negative glycerol polarization, yet is in fact consequence of the phase distortions introduced by water's RD effects, superimposing on a broadened water resonance.

Notice that in addition to phase distortions, solutes dissolved in hyperpolarized water show changing ^{1}H peak intensities, which vary non-monotonically with post-dissolution time. These intensity changes also originate in water's time-dependent RD effects, as can be appreciated from theoretical expectations that only considered such effects (Fig. 6, bottom). Indeed, in a similar way as RD shortens water's transverse magnetization lifetime, water-derived RF fields will also suppress the lifetimes associated to solute's transverse magnetizations that fall within water's line width. Solute signal intensities will thus progressively increase and sharpen as water's hyperpolarization decays. For similar reasons, solute signal intensities increase and sharpen progressively as a solute's resonance moves away from the water frequency.

In addition to these RD-derived effects, solute intensities will also be influenced by magnetization transfers from the hyperpolarized water *via* intermolecular NOEs for the non-labile solute protons, and *via* chemical exchanges for the labile ones. As the solutes involved are small molecules, NOEs will induce negative magnetization enhancements for a positive water hyperpolarization (*i.e.*, for propanol aliphatic and pyridine protons in Fig. 1, and for alanine's methyl in Fig. 2), while alanine's NH_3 signal will undergo positive – and, depending on the pH, more significant – polarization transfers as driven by water chemical exchanges. Unfortunately, an accurate quantitative interpretation of these absolute signal intensity changes is limited by data processing and experimental constraints. Data processing-wise, the accurate integration of the weak solute signals is hampered by the changing baselines arising from the much more intense hyperpolarized water resonance. At an experimental level, the solutes' mixed phase line shapes coupled to receiver deadtime effects, further complicate the analyses. Consequently, parameters related to enhancements, cross-relaxation, and chemical exchange rates could only be extracted from solute signal integrals at semi-quantitative levels.

To proceed with the solute intensity quantification, Gaussian best fits were first made to the overall water line shape, and these were used as baseline for calculating the solute's post-dissolution intensities (see SI Section S3 for further details). Thereafter, the aforementioned RD-induced phase and intensity distortions affecting the solute signals were compensated, using a correction corresponding to the inverse magnitude of the prefactor in eqn (11):

$$\left(\frac{i\Delta\omega}{\delta + i\Delta\omega}\right)^{2} = |A| e^{i\varphi};$$

$$|A| = \frac{\Delta\omega^{2}}{\left(\frac{|\lambda_{RD}| M^{w}}{2}\right)^{2} + |\lambda_{RD}| M^{w} \cdot \Delta\omega \cdot \sin(\psi) + \Delta\omega^{2}}; \quad (12)$$

$$\varphi = 2\mathrm{arctg}\left(\frac{\frac{|\lambda_{RD}| M^{w}}{2}\cos(\psi)}{\Delta\omega + \frac{|\lambda_{RD}| M^{w}}{2}\sin(\psi)}\right)$$

With these provisions at hand, analyses of the post-dissolution solute signal intensities in the spectra introduced in Fig. 1 and 2, led to the data points (circles) illustrated in Fig. 7. These data points were then fitted with classical Bloch–McConnell–Solomon equations relating the z-magnetizations of the water and solute protons

$$\begin{cases} \frac{dM_z^{w}}{dt} = -\frac{(M_z^{w} - M_0^{w})}{T_1^{w}} - n_s\sigma(M_z^{s} - M_0^{s}) - k_{ex}\frac{c_s}{c_w}M_z^{w} + k_{ex}M_z^{s} \ \text{(a)} \\ \frac{dM_z^{s}}{dt} = -\frac{(M_z^{s} - M_0^{s})}{T_1^{s}} - n_s\sigma(M_z^{w} - M_0^{w}) + k_{ex}\frac{c_s}{c_w}M_z^{w} - k_{ex}M_z^{s} \ \text{(b)} \end{cases} \quad (13)$$

where σ is the per-proton water $\Leftrightarrow$ solute intermolecular NOE at a given site, n_s are the number of protons at the site, k_{ex} is the chemical exchange constant (if relevant), T_1^{w}, T_1^{s} are the water's and solute's T_1 relaxation times, and c_s and c_w are the concentrations of solute and water molecules.

Based on these relations, the best fits of the water and solute (labile and nonlabile) signals introduced in Fig. 1 and 2, were obtained as summarized in Fig. 7. For the NOE-mediated transfer, non-labile protons in all samples exhibit weak intermolecular cross-relaxation rates from the hyperpolarized water – with values of $\sim 0.5 \times 10^{-4}$ s^{-1} and $\sim 2 \times 10^{-4}$ s^{-1} for propanol's and pyridine's protons, respectively, and of $\sim 1.1 \times 10^{-4}$ s^{-1} for alanine's methyl group. These values are comparable to reported heteronuclear ^{19}F–^{1}H intermolecular NOE rates,[21] as could be expected from ^{1}H–^{1}H intermolecular NOEs happening under comparable conditions. Alanine's NH_3 signal exhibited *ca.* 100-fold larger enhancements than the non-labile protons, arising from direct exchanges with the hyperpolarized water. Best fit of alanine's NH_3 enhancements resulted in an exchange rate $k_{ex} \approx 17$ s^{-1}; to further characterize this, complementary measurements on the same sample performed using chemical exchange saturation transfer (CEST) resulted in an exchange rate $k_{ex} \approx 20$ s^{-1} (SI, Section S3). Both of these values are consistent with previously reported exchange rates for alanine under comparable experimental conditions;[56] see Supporting Information for further details regarding these fits.

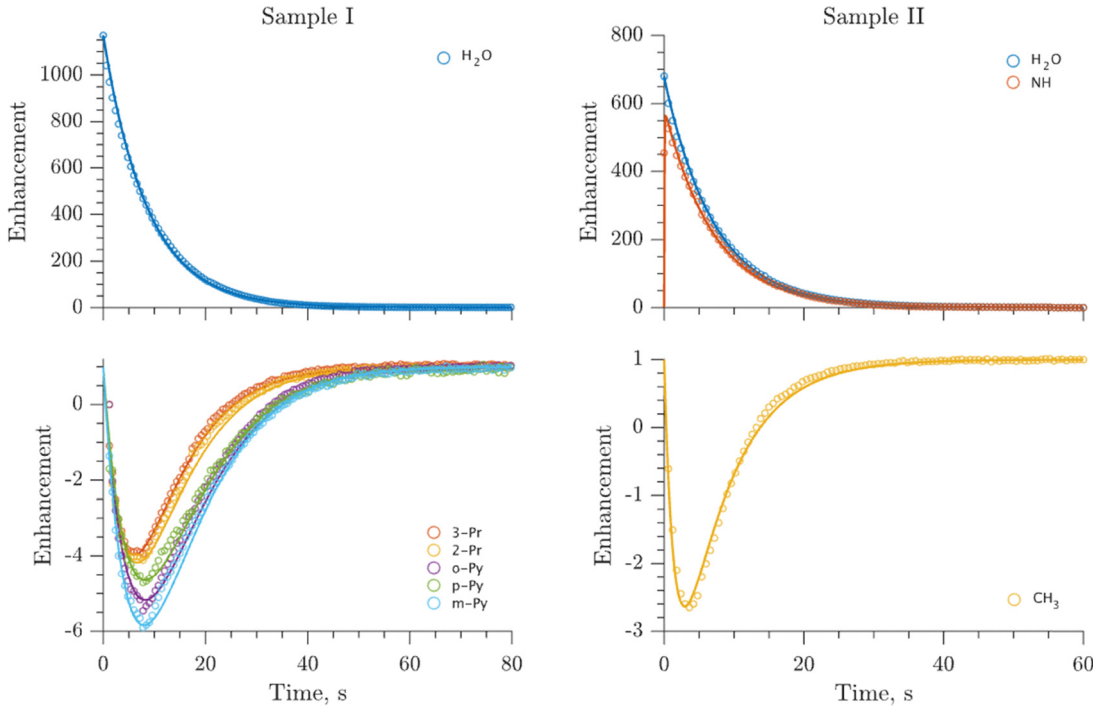

Fig. 7 Experimentally observed (circles) and best-fit enhancements (lines) deriving from the results obtained for sample I and sample II in the dissolution experiments shown in Fig. 1 and 2, after accounting for RD-driven amplitude and phase distortions (eqn (12)) and then solving eqn (13).

Discussion and conclusions

Hyperpolarized water has been shown as a powerful aid in enhancing the sensitivity of protein and nucleic acid experiments targeting labile NH groups.[24,55,57] Research is also evidencing the value of these HyperW experiments in sensitizing non-labile protons. The present work focused on less evident aspects that may arise in such experiments; foremost those driven by the unusually strong radiation damping effects that the highly polarized water resonance will impart both on its own spin dynamics, and on that of signals from co-dissolved solutes. For the latter case, analytical treatments and numerical simulations show that the spectral overlap between the RD-broadened water signal and the solute ^{1}H resonances lead to multiple measurable distortions in the phase, line width and amplitude of the ^{1}H peaks – even for non-labile sites. These distortions will change over time as the water hyperpolarization decays, they will be influenced by the characteristics of the detection circuit used to collect the NMR spectra, as well as by cross-relaxation and exchange effects. The ensuing calculations and derivations ended up in full agreement with experimental observations monitoring the solvent and solute line shapes of both labile and non-labile protons, in findings that highlight some hitherto ignored complexities that affect this kind of experiments.

The present study focused on line shapes arising from short, single-pulse 1D ^{1}H NMR acquisitions. However, also other experiments can be significantly affected by RD effects in hyperpolarized systems. A large body of recent research has focused on hyperpolarized metastable states leading to spontaneous, pulse-free maser-like emissions;[58,59] gradient applications on hyperpolarized systems can also lead to chaotic dynamics in simple one-pulse acquisitions.[60] These are all interesting instances where RD-mediated interactions between solutes and hyperpolarized water, remain to be researched. Another significant area waiting to be explored involves 2D homo- and heteronuclear HyperW experiments, where hitherto neglected effects like those described in this study are also expected to arise. Also the use of selective excitation pulses may result in an additional suppression or enhancement of solute signals due to the RD field, and therefore to exacerbate or attenuate the effects here described. Complex RD interactions are also expected when applying dissolution DNP on systems more complicated than water, where multiple chemically inequivalent sites might couple to one another non-linearly *via* the receiving circuit. We have also found that rapid repetitive pulsing along the lines often used in hyperpolarized NMR imaging acquisitions,[61,62] may also elicit interesting RD-related effects. Investigations on some of these interesting phenomena will be reported in an upcoming publication.

Conflicts of interest

There are no conflicts to declare.

Data availability

Much of the data that support the findings of this study are available in the main text and supplementary information (SI) files. Supplementary information: detailing demagnetizing

field and temperature corrections, additional simulation and experimental details, fits of the solutes' enhancements and CEST experiments. See DOI: https://doi.org/10.1039/d6cp00956e.

The raw data are available from the corresponding author upon reasonable request.

Acknowledgements

This work was supported by the Israel Science Foundation (grant 1874/22), the Minerva Foundation, the NSF-BSF program (grant 2023-705), ERC Advanced Grant Project 101200719 ''SteadyNMR'', and the Perlman Family Foundation. DA acknowledges the Weizmann Institute of Science for a Dean fellowship and the Israel Ministry of Absorption (No. 151989) for a postdoctoral fellowship; LF is the incumbent of The Bertha and Isadore Gudelsky Professorial Chair.

References

1 C. P. Slichter, *Principles of Magnetic Resonance*, Springer Berlin Heidelberg, Berlin, Heidelberg, 1978, vol. 1.
2 T. D. W. Claridge, *High-Resolution NMR Techniques in Organic Chemistry*, Elsevier, 2016.
3 J. J. Keeler, *Understanding NMR Spectroscopy*, Wiley, Chichester, 2nd edn, 2011.
4 J. Cavanagh, W. J. Fairbrother, I. Arthur G. Palmer, M. Rance and N. J. Skelton, *Protein NMR Spectroscopy: Principles and Practice*, Academic Press, 2007.
5 M. J. Duer, *Introduction to solid-state NMR spectroscopy*, Blackwell, Oxford, UK, Malden, MA, 2004.
6 J. Eills, D. Budker, S. Cavagnero, E. Y. Chekmenev, S. J. Elliott, S. Jannin, A. Lesage, J. Matysik, T. Meersmann, T. Prisner, J. A. Reimer, H. Yang and I. V. Koptyug, Spin Hyperpolarization in Modern Magnetic Resonance, *Chem. Rev.*, 2023, **123**, 1417–1551.
7 C. R. Bowers and D. P. Weitekamp, Parahydrogen and synthesis allow dramatically enhanced nuclear alignment, *J. Am. Chem. Soc.*, 1987, **109**, 5541–5542.
8 T. G. Walker and W. Happer, Spin-exchange optical pumping of noble-gas nuclei, *Rev. Mod. Phys.*, 1997, **69**, 629–642.
9 A. W. Overhauser, Polarization of Nuclei in Metals, *Phys. Rev.*, 1953, **92**, 411–415.
10 T. Wenckebach, *Essentials of Dynamic Nuclear Polarization, Spindrift Publications*, The Netherlands, 2016.
11 A. Abragam and M. Goldman, Principles of dynamic nuclear polarisation, *Rep. Prog. Phys.*, 1978, **41**, 395–467.
12 ed. V. K. Michaelis, R. G. Griffin, B. Corzilius and S. Vega, *Handbook of high field dynamic nuclear polarization*, Wiley, Chichester, 2020.
13 J. H. Ardenkjær-Larsen, B. Fridlund, A. Gram, G. Hansson, L. Hansson, M. H. Lerche, R. Servin, M. Thaning and K. Golman, Increase in signal-to-noise ratio of >10,000 times in liquid-state NMR, *Proc. Natl. Acad. Sci. U. S. A.*, 2003, **100**, 10158–10163.
14 S. J. Nelson, D. Vigneron, J. Kurhanewicz, A. Chen, R. Bok and R. Hurd, DNP-Hyperpolarized 13C Magnetic Resonance Metabolic Imaging for Cancer Applications, *Appl. Magn. Reson.*, 2008, **34**, 533–544.
15 J. Kurhanewicz, D. B. Vigneron, K. Brindle, E. Y. Chekmenev, A. Comment, C. H. Cunningham, R. J. DeBerardinis, G. G. Green, M. O. Leach, S. S. Rajan, R. R. Rizi, B. D. Ross, W. S. Warren and C. R. Malloy, Analysis of Cancer Metabolism by Imaging Hyperpolarized Nuclei: Prospects for Translation to Clinical Research, *Neoplasia*, 2011, **13**, 81–97.
16 G. Mathies, S. Jannin and L. Frydman, Hyperpolarization: From toy to tool, and back to toy, *J. Magn. Reson. Open*, 2025, **23**, 100202.
17 M. D. Lingwood, T. A. Siaw, N. Sailasuta, O. A. Abulseoud, H. R. Chan, B. D. Ross, P. Bhattacharya and S. Han, Hyperpolarized Water as an MR Imaging Contrast Agent: Feasibility of in Vivo Imaging in a Rat Model, *Radiology*, 2012, **265**, 418–425.
18 T. Harris, O. Szekely and L. Frydman, On the Potential of Hyperpolarized Water in Biomolecular NMR Studies, *J. Phys. Chem. B*, 2014, **118**, 3281–3290.
19 J. H. Ardenkjaer-Larsen, C. Laustsen, S. Bowen and R. Rizi, Hyperpolarized H2O MR angiography, *Magn. Reson. Med.*, 2014, **71**, 50–56.
20 Q. Stern, J. Milani, B. Vuichoud, A. Bornet, A. D. Gossert, G. Bodenhausen and S. Jannin, Hyperpolarized Water to Study Protein–Ligand Interactions, *J. Phys. Chem. Lett.*, 2015, **6**, 1674–1678.
21 J. Kim, M. Liu, H.-Y. Chen and C. Hilty, Determination of Intermolecular Interactions Using Polarization Compensated Heteronuclear Overhauser Effect of Hyperpolarized Spins, *Anal. Chem.*, 2015, **87**, 10982–10987.
22 A. Bornet, M. Maucourt, C. Deborde, D. Jacob, J. Milani, B. Vuichoud, X. Ji, J.-N. Dumez, A. Moing, G. Bodenhausen, S. Jannin and P. Giraudeau, Highly Repeatable Dissolution Dynamic Nuclear Polarization for Heteronuclear NMR Metabolomics, *Anal. Chem.*, 2016, **88**, 6179–6183.
23 J. Kim, M. Liu and C. Hilty, Modeling of Polarization Transfer Kinetics in Protein Hydration Using Hyperpolarized Water, *J. Phys. Chem. B*, 2017, **121**, 6492–6498.
24 D. Kurzbach, E. Canet, A. G. Flamm, A. Jhajharia, E. M. M. Weber, R. Konrat and G. Bodenhausen, Investigation of Intrinsically Disordered Proteins through Exchange with Hyperpolarized Water, *Angew. Chem., Int. Ed.*, 2017, **56**, 389–392.
25 O. Szekely, G. L. Olsen, I. C. Felli and L. Frydman, High-Resolution 2D NMR of Disordered Proteins Enhanced by Hyperpolarized Water, *Anal. Chem.*, 2018, **90**, 6169–6177.
26 K. W. Lipsø, E. S. S. Hansen, R. S. Tougaard, C. Laustsen and J. H. Ardenkjaer-Larsen, Dynamic coronary MR angiography in a pig model with hyperpolarized water, *Magn. Reson. Med.*, 2018, **80**, 1165–1169.
27 J. Kim, R. Mandal and C. Hilty, Observation of Fast Two-Dimensional NMR Spectra during Protein Folding Using

Polarization Transfer from Hyperpolarized Water, *J. Phys. Chem. Lett.*, 2019, **10**, 5463–5467.
28 M. Novakovic, G. L. Olsen, G. Pintér, D. Hymon, B. Fürtig, H. Schwalbe and L. Frydman, A 300-fold enhancement of imino nucleic acid resonances by hyperpolarized water provides a new window for probing RNA refolding by 1D and 2D NMR, *Proc. Natl. Acad. Sci. U. S. A.*, 2020, **117**, 2449–2455.
29 O. Szekely, G. L. Olsen, M. Novakovic, R. Rosenzweig and L. Frydman, Assessing Site-Specific Enhancements Imparted by Hyperpolarized Water in Folded and Unfolded Proteins by 2D HMQC NMR, *J. Am. Chem. Soc.*, 2020, **142**, 9267–9284.
30 C. Hilty, D. Kurzbach and L. Frydman, Hyperpolarized water as universal sensitivity booster in biomolecular NMR, *Nat. Protoc.*, 2022, **17**, 1621–1657.
31 L. M. Epasto, K. Che, F. Kozak, A. Selimovic, P. Kadeřávek and D. Kurzbach, Toward protein NMR at physiological concentrations by hyperpolarized water—Finding and mapping uncharted conformational spaces, *Sci. Adv.*, 2022, **8**, eabq5179.
32 N. Pradhan and C. Hilty, Cross-Polarization of Insensitive Nuclei from Water Protons for Detection of Protein–Ligand Binding, *J. Am. Chem. Soc.*, 2024, **146**, 24754–24758.
33 Y. Zhao, M. H. Lerche, M. Karlsson, R. B. Olin, E. S. S. Hansen, M. Aastrup, M. Redda, C. Laustsen, L. G. Hanson and J. H. Ardenkjær-Larsen, Hyperpolarized Water for Coronary Artery Angiography and Whole-Heart Myocardial Perfusion Quantification, *Tomography*, 2024, **10**, 1113–1122.
34 Y. Lee and J. Kim, Hyperpolarized water via dissolution dynamic nuclear polarization: Applications in biomolecular NMR, *Appl. Spectrosc. Rev.*, 2024, **59**, 1322–1343.
35 M. Zachrdla, E. Turhan, M. Bučková, R. Hänsel-Hertsch, L. Trantírek and D. Kurzbach, Hyperpolarized NMR Reveals Low-Populated Folding Intermediates in DNA, *J. Am. Chem. Soc.*, 2025, **147**, 46563–46572.
36 D. Brandis, E. Turhan, M. Zachrdla and D. Kurzbach, Residue-Resolved Liquid-State Hyperpolarized NMR of Peptide Condensate Surfaces, *J. Am. Chem. Soc.*, 2025, **147**, 36920–36927.
37 F. Hecker, K. Teilum, A. Capozzi and M. H. Lerche, Residue-Specific Signatures of Structural Water Identified by Dissolution Dynamic Nuclear Polarization with UV-Generated Radicals, *Angew. Chem., Int. Ed.*, 2026, e23739.
38 A. Vlassenbroek, J. Jeener and P. Broekaert, Radiation damping in high resolution liquid NMR: A simulation study, *J. Chem. Phys.*, 1995, **103**, 5886–5897.
39 J.-H. Chen, A. Jerschow and G. Bodenhausen, Compensation of radiation damping during selective pulses in NMR spectroscopy, *Chem. Phys. Lett.*, 1999, **308**, 397–402.
40 M. P. Augustine, Transient properties of radiation damping, *Prog. Nucl. Magn. Reson. Spectrosc.*, 2002, **40**, 111–150.
41 D. Abergel, A. Louis-Joseph and J.-Y. Lallemand, Self-sustained Maser oscillations of a large magnetization driven by a radiation damping-based electronic feedback, *J. Chem. Phys.*, 2002, **116**, 7073–7080.
42 P. Giraudeau, N. Müller, A. Jerschow and L. Frydman, 1H NMR noise measurements in hyperpolarized liquid samples, *Chem. Phys. Lett.*, 2010, **489**, 107–112.
43 J. Schlagnitweit, S. W. Morgan, M. Nausner, N. Müller and H. Desvaux, Non-Linear Signal Detection Improvement by Radiation Damping in Single-Pulse NMR Spectra, *Chem. Phys. Chem.*, 2012, **13**, 482–487.
44 H. Desvaux, Non-linear liquid-state NMR, *Prog. Nucl. Magn. Reson. Spectrosc.*, 2013, **70**, 50–71.
45 M. T. Pöschko, J. Schlagnitweit, G. Huber, M. Nausner, M. Horničáková, H. Desvaux and N. Müller, On the Tuning of High-Resolution NMR Probes, *Chem. Phys. Chem.*, 2014, **15**, 3639–3645.
46 V. F. T. J. Chacko, A. Louis-Joseph and D. Abergel, Multimode Masers of Thermally Polarized Nuclear Spins in Solution NMR, *Phys. Rev. Lett.*, 2024, **133**, 158001.
47 K. A. Marr and A. Jerschow, Avoiding broadband radiation damping effects in NOESY spectra, *J. Magn. Reson. Open*, 2025, **23**, 100203.
48 R. Ishima, Effects of radiation damping for biomolecular NMR experiments in solution: a hemisphere concept for water suppression, *Concepts Magn. Reson., Part A*, 2015, **44A**, 252–262.
49 S. Katsikis, I. Marin-Montesinos, M. Pons, C. Ludwig and U. L. Günther, Improved Stability and Spectral Quality in Ex Situ Dissolution DNP Using an Improved Transfer Device, *Appl. Magn. Reson.*, 2015, **46**, 723–729.
50 M. H. Levitt, Demagnetization field effects in two-dimensional solution NMR, *Concepts Magn. Reson.*, 1996, **8**, 77–103.
51 H. E. Gottlieb, V. Kotlyar and A. Nudelman, NMR Chemical Shifts of Common Laboratory Solvents as Trace Impurities, *J. Org. Chem.*, 1997, **62**, 7512–7515.
52 D. Abergel, Chaotic solutions of the feedback driven Bloch equations, *Phys. Lett. A*, 2002, **302**, 17–22.
53 X. Mao, J. Guo and C. Ye, Nuclear-magnetic-resonance lineshape theory in the presence of radiation damping, *Phys. Rev. B: Condens. Matter Mater. Phys.*, 1994, **49**, 15702–15711.
54 M. Guéron, A coupled resonator model of the detection of nuclear magnetic resonance: Radiation damping, frequency pushing, spin noise, and the signal-to-noise ratio, *Magn. Reson. Med.*, 1991, **19**, 31–41.
55 G. Olsen, E. Markhasin, O. Szekely, C. Bretschneider and L. Frydman, Optimizing water hyperpolarization and dissolution for sensitivity-enhanced 2D biomolecular NMR, *J. Magn. Reson.*, 2016, **264**, 49–58.
56 M. Zachrdla, E. Turhan, C. Pötzl, A. Sadet, P. R. Vasos and D. Kurzbach, Hyperpolarized nuclear Overhauser enhancement of alanine methyl groups by doubly relayed proton exchange, *J. Magn. Reson.*, 2024, **364**, 107727.
57 P. Kadeřávek, F. Ferrage, G. Bodenhausen and D. Kurzbach, High-Resolution NMR of Folded Proteins in Hyperpolarized Physiological Solvents, *Chem. – Eur. J.*, 2018, **24**, 13418–13423.
58 I. A. Trofimov, O. G. Salnikov, A. N. Pravdivtsev, H. de Maissin, A. P. Yi, E. Y. Chekmenev, J.-B. Hövener,

A. B. Schmidt and I. V. Koptyug, Through-bond and through-space radiofrequency amplification by stimulated emission of radiation, *Commun. Chem.*, 2024, **7**, 235.

59 O. G. Salnikov, I. A. Trofimov, A. N. Pravdivtsev, K. Them, J.-B. Hövener, E. Y. Chekmenev and I. V. Koptyug, Through-Space Multinuclear Magnetic Resonance Signal Enhancement Induced by Parahydrogen and Radiofrequency Amplification by Stimulated Emission of Radiation, *Anal. Chem.*, 2022, **94**, 15010–15017.

60 Y.-Y. Lin, N. Lisitza, S. Ahn and W. S. Warren, Resurrection of Crushed Magnetization and Chaotic Dynamics in Solution NMR Spectroscopy, *Science*, 2000, **290**, 118–121.

61 J. G. Skinner, G. J. Topping, L. Nagel, I. Heid, C. Hundshammer, M. Grashei, F. H. A. van Heijster, R. Braren and F. Schilling, Spectrally selective bSSFP using off-resonant RF excitations permits high spatiotemporal resolution 3D metabolic imaging of hyperpolarized [1-13 C]Pyruvate-to-[1-13 C]lactate conversion, *Magn. Reson. Med.*, 2023, **90**, 894–909.

62 Z. Wang, M. Grashei, J. Fischer, S. Sühnel, N. Setzer, M. Awenius, A. Korzowski, A. C. Özen, M. Zaitsev, M. Bock, F. Schilling, A. B. Schmidt and C. A. Müller, Radial multi-echo bSSFP and IDEAL chemical shift separation in k-space for high-speed 3D hyperpolarized 13C metabolic MRI, *Magn. Reson. Med.*, 2025, **94**, 2190–2200.